This manuscript was accepted by Rev. Sci.Instrum. Click here to see the version of record.

High-frequency measurements of thermophysical properties of thin films using a modified broad-band frequency domain thermoreflectance approach

Mohammadreza Shahzadeh [1], Mizanur Rahman [2], Olav Hellwig [3,4], Simone Pisana [1,2,]*

1. Department of Electrical Engineering and Computer Science, York University, 4700 Keele Street, Toronto ON, M3J 1P3, Canada

2. Department of Physics and Astronomy, York University, 4700 Keele Street, Toronto ON, M3J 1P3, Canada

3. Institute of Physics, Technische Universität Chemnitz, Reichenhainer Straße 70, 09126 Chemnitz, Germany

4. Institute of Ion Beam Physics and Materials Research, Helmholtz-Zentrum Dresden-Rossendorf, Bautzner Landstraße 400, 01328 Dresden, Germany

[*] Corresponding Author: simone.pisana@lassonde.yorku.ca

Abstract

In this work we present the implementation of a new method to perform high-frequency thermoreflectance measurements on thin films. The so-called Differential Broad-Band Frequency Domain Thermoreflectance (DBB-FDTR) method follows BB-FDTR developed previously [K.T. Regner, S. Majumdar, and J. A. Malen, Rev. Sci. Instrum. 84, 064901 (2013)], without the use of expensive electro-optic modulators. Two techniques are introduced to recover the thermal phase of interest and to separate it from the unwanted instrumental contributions to the recorded phase. Measuring a differential thermal phase by either varying the spot size or offsetting the pump and probe beams, the thermophysical properties of materials can be extracted. This approach enables the study of nanoscale heat transport where non-equilibrium phenomena are dominating.

Keywords: Thermoreflectance, FDTR, Thermal Conductivity

Introduction

With the advances in high-current sub-micron electronic devices, heat transfer and heat dissipation have become crucially important. Heat transfer is particularly problematic in nanoscale electronic devices, where heat typically travels through several sub-micron layers and interfaces before reaching a bulk-like heat sink. The resistance to heat transfer at the interfaces can become comparable to, or even dominate, the heat resistance through sub-micron films, and lead to heat accumulation within the device. This temperature rise can in turn result in degradation of the materials and lowering of the device performance and endurance. In order to engineer interfaces with desirable thermal characteristics and predict their heat transport behavior, the thermophysical properties of the interfaces and the materials forming the interfaces need to be known. Moreover, as the thickness of the layered materials becomes comparable to the mean free path (MFP) of the heat carriers, the transport will be non-diffusive, and the heat carriers will not be in thermodynamic equilibrium everywhere. In this case, understanding how heat transport departs from Fourier theory is important to adequately model heat transport in electronic devices. To do so, metrology techniques that allow the investigation of heat transport over length scales that approach the carriers' MFP are essential. This is typically accomplished by either imposing heat sources smaller than the MFP and/or inducing thermal waves that decay over shorter distances than the MFP.

Different methods have been developed to measure the thermophysical properties of materials and interfaces. Firstly described and implemented by Cahill and co-workers [1,2], the 3ω method employs a microfabricated metallic line that acts as both heater and thermometer on the sample under study [3]. However despite its simplicity, the most important limitation of the 3ω method is that the modulation frequency is typically limited to 100 kHz [4]; this limits the thermal penetration depth of the heat waves and the ability to characterize heat transport at small length scales. The penetration depth is expressed as $\ell = \sqrt{\lambda/\pi C f}$, where λ is the thermal conductivity, C is the volumetric heat capacity and f is the modulation frequency. Therefore a modulation frequency of 100 kHz leads to a thermal penetration depth of 17 μm in Si, limiting the access to transport over sub-micron length scales. To reach $\ell = 1$ μm in Si, $f > 28$ MHz is necessary. We note, however, that even steady-state approaches can peer into non-diffusive transport when the heat sources are sufficiently small [5].

Advances in optics and photonics have led to the development of optical metrology systems based on pump and probe techniques such as time-domain thermoreflectance (TDTR) and frequency-domain thermoreflectance (FDTR). Their popularity is driven in part by the simpler sample preparation, which unlike thermometry approaches do not require microfabrication or response calibration. FDTR and TDTR, along with their related techniques, allow in some cases simultaneous measurement of several thermal properties of bulk and thin film materials. In FDTR and TDTR, a thin metallic layer is deposited on the sample surface, which acts as a transducer, serving as both heater and thermometer. Changes in the transducer's optical reflectivity as function of temperature (thermoreflectance) allows a probing laser to sense the temperature changes induced by a pump laser beam.

Schmidt and co-workers implemented FDTR to obtain heat transport measurements with a modulation frequency of up to 20 MHz [6, 7]. By extending the FDTR technique, Yang and co-workers produced thermal maps of different thermophysical properties [8]. The same technique was used by Yang and co-workers to measure the in-plane thermal conductivity and the thermal boundary conductance (TBC) of a metal/graphene/SiO_2 structure by increasing the pump modulation frequency up to 50 MHz [9]. Moreover, techniques such as beam offset FDTR have been employed to measure the thermo-physical properties of anisotropic materials [10, 11]. We recently demonstrated how further combining a beam-offset approach with high frequency FDTR performed using small spot sizes can lead to lower uncertainties in the measurement of thermally anisotropic samples [12].

Most FDTR measurements are limited to around 20 MHz. At frequencies larger than 20 MHz, the SNR drops significantly due to the decrease of the signal (surface temperature oscillations vary as $f^{1/2}$ for the 1D case) and increase in noise (mostly coherent RF noise picked up by the electrical cables). Figure 1 shows the amplitude of the thermal signal and noise in a typical FDTR measurement, where the SNR rapidly drops above 10 MHz. We will show here how we have extended the frequency range to 100 MHz with careful choice of the experimental conditions, which is the limit of the HF2LI lock-in amplifier we use. However, further extending the frequency this way is increasingly difficult as the SNR lowers.

To overcome this limitation, Regner and co-workers implemented a Broad-Band version of the FDTR, the so-called BB-FDTR, and increased the pump modulation frequency up to 200 MHz [13]. BB-FDTR was used to determine the contribution of

This manuscript was accepted by Rev. Sci.Instrum. Click here to see the version of record.

phonons with different MFPs to the thermal conductivity in different metallic and non-metallic materials [14-16].

In order to improve the SNR of FDTR, Regner and co-workers used a heterodyning approach to shift the detection of the high-frequency thermal signal to a lower frequency before optical detection, thereby limiting RF noise in the detection cabling and electronics. More specifically, in their work, an external electro-optic modulator (EOM) modulates the output of the pump laser at f_1 while the CW probe laser measures the surface temperature of the sample (Figure 2a). Then another EOM working at f_2 is placed before the detector and modulates the probe light reflected from the sample, generating heterodyne frequencies at $f_1 \pm f_2$. The component of $f_1 - f_2$ is then detected. In FDTR the quantity of interest is the thermal phase lag of the temperature of the sample with respect to the heat flux generated by the pump beam. To isolate the thermal phase from other experimental sources of phase offset, a reference measurement is needed (described in more detail below) [13]. Figure 1 shows the SNR for a BB-FDTR measurement based on the heterodyning approach introduced by Regner and co-workers. Using a heterodyne frequency of 100 kHz, the SNR becomes smaller than 10 at around 170 MHz in comparison with typical FDTR where this happens at around 70 MHz (Figure 1). The test sample in this case is a multi-layered Al(59nm)/SiO_2(150nm)/Si sample, under incident powers of 10 mW and 18 mW of 515 nm and 785 nm, respectively with rms spot size of ~ 1.4 μm. The BB-FDTR technique developed by Regner and co-workers requires the use of two EOMs, which add significantly to the cost of implementation.

Regner and co-workers proposed an alternative placement for the heterodyning EOM: on the probe path before the sample, in a similar way as the pump beam EOM. However, in this case, they did not propose a method to recover the thermal phase of interest from the unwanted instrumental contributions to the measured phase. Herein, we resolve this issue by presenting two different techniques to perform BB-FDTR measurements beyond 100 MHz. Since the laser beams are modulated before the sample, both methods eliminate the use of EOMs altogether, by using analog modulated pump and probe lasers. We recover the thermal phase of interest through a differential approach. We also present another approach to extend the frequency capabilities of typical FDTR implementations to 100 MHz by maximizing the signal and mitigating noise without heterodyning. These approaches provide economical means to characterizing heat transport at submicron length scales.

This manuscript was accepted by Rev. Sci.Instrum. Click here to see the version of record.

DBB-FDTR Implementation

Schematics for two approaches of the differential BB-FDTR (DBB-FDTR) setup are shown in Figure 2b and 2c. A two-channel function generator (Anritsu-MG3740A) is used to modulate the intensities of the pump and probe lasers (Omicron A350 operating at 515 nm and 785 nm) at f_1 and f_2, respectively. Optical isolators (Conoptics M711A and M712B) are used to minimize back-reflections that can destabilize the laser sources. We also avoid back-reflections of the probe from entering the pump, and vice versa, to prevent inadvertent heterodyning through optical cavity modulation. Half-wave plates, a polarizing beam splitter and a quarter-wave plate are used to ensure maximum light throughput in a coaxial setup as light reaches the sample and is reflected back towards the detector. A 40X objective (Olympus RMS40X) is used to focus the beams on the surface of the sample. The small spot sizes obtained ($\sim$1.5 μm) improve the signal and improve sensitivity to in-plane thermal transport. The surface temperature of the sample oscillates at the frequency of pump (i.e. f_1), as the pump light is absorbed on the transducer. The probe laser operating at frequency f_2 samples the temperature response from the transducer by thermoreflectance, i.e. changes of reflectivity due to the surface temperature. The heterodyne frequencies of $f_1 \pm f_2$ generated on the surface of the sample by mixing the pump and probe signals are then measured by a photodetector (Thorlabs PDA8A). We note that the photodetector's 50 MHz bandwidth is not necessary for DBB-FDTR, as we typically measure the low-frequency heterodyne component where the noise is at a minimum and limited by the detector. A lock-in amplifier (Zurich Instruments HF2LI) locked at the frequency $f_1 - f_2$ is used to demodulate the signal. We note that a high-frequency lock-in amplifier is not necessary to implement DBB-FDTR.

The phase measured at the lock-in amplifier has contributions from the thermal, optical and electrical phases with respect to a reference phase from the signal generator, i.e. $\theta_1 = \theta_{Thermal} + \theta_{Optical} + \theta_{Electrical} + \theta_{ref}$. Typically in FDTR and BB-FDTR, after performing the thermal measurement θ_1 (a measurement that includes the thermal phase lag of interest) a non-thermal measurement θ_2 is used to recover the thermal phase of interest from other unwanted phases; i.e. $\theta_2 = \theta_{Optical} + \theta_{Electrical} + \theta_{ref}$. Therefore $\theta_1 - \theta_2 = \theta_{Thermal}$. The non-thermal measurement is typically achieved by replacing a filter in front of the detector in order to measure the modulated pump, rather than the probe. This approach is not viable when the pump and probe are

This manuscript was accepted by Rev. Sci.Instrum. Click here to see the version of record.

directly modulated (as we do here), as the pump is not heterodyned and there is no signal at $f_1 - f_2$ for the measurement θ_2.

In the DBB-FDTR presented here, after performing the first thermal measurement ($\theta_1 = \theta_{1,Thermal} + \theta_{1,Optical} + \theta_{1,Electrical} + \theta_{1,ref}$), another thermal measurements is performed either at a different focal point (using a Thorlabs KPZNFL5 piezo translational stage, depicted in Figure 2b), or on the same focal point but with an offset between the pump and probe beams (using a Newport TRA12CC actuator, depicted in Figure 2c). In this case, $\theta_2 = \theta_{2,Thermal} + \theta_{2,Optical} + \theta_{2,Electrical} + \theta_{2,ref}$. Key to our approach is to perform two thermal measurements that yield a sufficiently different thermal response, but otherwise have identical instrumental phases. Subtracting these two thermal measurements gives a differential thermal phase (DTP) that can be analyzed to extract the thermal parameters of interest.

As it will be shown later, accurate knowledge of the pump and probe spot sizes or the offset between the pump and probe spots is important to reduce errors. To this end, the spot sizes are measured locally every time a DBB-FDTR measurement is made. We measure the spot sizes by analyzing the convoluted response obtained by scanning the relative offset between the Gaussian pump and probe beams [10]. These measurements are performed at 43 MHz to minimize the effects of in-plane thermal transport on the measured profile, and further increasing the modulation frequency has no effect on the spot size obtained. The results obtained in this way have been checked with a razor profiler for consistency.

In focal DBB-FDTR (Figure 2b), two thermal measurements are performed in the same frequency range at two different focal positions. Any frequency-dependent variation to the electrical phase is common between the measurements performed at the two focal points, since the frequency range is identical, and therefore $\theta_{1,Electrical} = \theta_{2,Electrical}$. Moreover, since the beams are modulated with the same source, $\theta_{1,ref} = \theta_{2,ref}$. The optical phase shift for each beam travelling in free space is $\theta = kd$, where d is the distance travelled and k is the modulation wavenumber, so the optical phase shift difference between pump ($\theta_P = k_P d$) and probe ($\theta_S = k_S d$) is $\frac{2\pi}{c}(f_P - f_S)d$, where f_P and f_S are frequencies of modulation for pump and probe beams. By choosing a heterodyne frequency of 100 kHz and given that the sample is typically defocused by shifting it over a distance of 7 μm, the optical phase difference is ~

This manuscript was accepted by Rev. Sci.Instrum. Click here to see the version of record.

10^{-8} deg. Therefore, $\theta_{1,Optical} - \theta_{2,Optical} \sim 0$, and the Differential Thermal Phase (DTP) then can be extracted by calculating $\theta_1 - \theta_2 = \theta_{1,Thermal} - \theta_{2,Thermal}$.

By fitting the difference in the solutions of the diffusive heat equation calculated at the two focal points to the measured DTP, the unknown thermophysical properties can be extracted. In general, the surface temperature fluctuations in the frequency domain can be evaluated using:

$$\Delta T(f) = \frac{2\pi}{A_s}\int_0^\infty G(f,k)P(k)S(k)kdk \quad (1)$$

where $G(f,k)$ is the Hankel transform of the Green's function solution for the temperature response due to a sinusoidal oscillating point source of unit strength, $P(k)$ and $S(k)$ are the Hankel transforms of Gaussian intensity profiles of the pump and probe beams, and A_s is the total intensity of the probe beam. Expressions for $G(f,k)$ can be found elsewhere for multi-layered samples considering thermal anisotropy [17, 18].

For the two methods introduced in this work to perform DBB-FDTR (focal and offset DBB-FDTR), the relations for $P(k)$ and $S(k)$ in Eq. (1) are specified differently. In focal DBB-FDTR, the pump and probe beams are concentric [6, 17]. Therefore in this case, $P(k)$ and $S(k)$ in Eq. (1) are expressed in a manner similar to typical TDTR, FDTR or BB-FDTR treatments [13]. The surface temperature fluctuation of the sample in the offset DBB-FDTR approach is different from the focal DBB-FDTR, as the Hankel transform of the intensity profile of the probe beam with an offset $S(k)$ needs to be modified. Feser and Cahill have provided an efficient way of calculating the thermal response for non-concentric pump and probe beams [10].

Extension of FDTR to High Frequency

One alternative method to increase the modulation frequency in FDTR while maintaining a sufficient SNR, is briefly described here. This method doesn't rely on heterodyning to perform measurements at a frequency where RF noise is minimized. Instead, reducing the spot sizes leads to increases in the signal amplitude, due to the increase in the magnitude of the surface temperature oscillations. In this case, care must be taken to ensure that the temperature oscillations do not yield a nonlinear

thermoreflectance response, that the local temperature rise is not above the desired value or result in irreversible sample modification. This can be done by checking that the thermal phase obtained is power-independent. Reducing the spot size also increases potential sources of error in accurately determining the spot size, therefore local spot size measurements for each sample are important. A lock-in amplifier capable of demodulating the signal at the selected frequency range is needed. Here we use a Zurich Instruments HF2LI lock-in amplifier. Although the nominal bandwidth of the HF2LI is 50 MHz, and the signal strength is reduced beyond this, the instrument is capable of demodulating signals up to 100 MHz. The use of several ferrite cores on the signal cables reduces coherent noise. In spite of the bandwidth limitations of both the lock-in amplifier and photodetector, we can perform measurements to ~100 MHz.

In order to further cancel residual RF noise in the detected thermal signal, we used a mathematical approach, since the noise is coherent with the signal. We therefore subtract the measured noise vector (obtained by preventing the modulated probe laser light from reaching the detector) from the measured signal vector, to obtain the thermal signal. In practice, for the noise measurement, since we want to keep any source of coherent noise coming from the modulation process without directly detecting the modulated probe light, the probe laser is negatively biased to below the lasing threshold, but its modulation input is left on. This procedure facilitates automating the process of measuring the noise vector, as it is simpler to implement than steering or filtering the probe light. The noise measurement was averaged to obtain a value with sufficient accuracy. We note that using small spot sizes not only increases the thermal signal, but also reduces the sources of coherent noise since the amplitudes of the voltage signals used to modulate the lasers while maintaining a sufficiently strong signal thermal signal are lowered.

Sample Preparation and Sensitivity Analysis

Three different samples have been studied in this paper. The samples were prepared by sputter deposition of Al thin films on various substrates. Sample 1 consists of Al(59nm)/SiO_2(150nm)/Si, sample 2 is Al(59nm)/Si and sample 3 is Al(59nm)/MgO. The thickness of the layers was determined by X-Ray reflectivity and the in-plane thermal conductivity of the Al transducers were determined by 4-point probe electrical conductivity and applying the Wiedemann-Franz Law. The thermophysical parameters of the samples are listed in Table 1. The values for the

This manuscript was accepted by Rev. Sci.Instrum. Click here to see the version of record.

out-of-plane thermal conductivity and volumetric heat capacity were taken from the literature.

In order to investigate how sensitive the thermal phase is to different parameters, a sensitivity analysis is performed. The definition typically used for the sensitivity is the logarithmic derivative of the phase with respect to the changes of a given parameter [13]. Here we prefer to calculate the absolute difference in the thermal phase when the parameter of interest is changed by 10%. This definition leads to a direct insight into whether a quantity is measurable or not by comparing the phase sensitivity to the typical phase noise of the measurement.

Figure 3a and 3b show the sensitivity analysis and the modeled DTP for Al/SiO_2/Si for focal DBB-FDTR. The modeled DTP is highly dependent on the spot sizes used in the focal DBB-FDTR configuration. The DTP increases by increasing the difference between the first and the second measurement's rms spot sizes, however one should note that the thermal signal magnitude decreases at larger spot sizes due to the reduction in surface temperature oscillations.

Figure 3c and 3d show the sensitivity analysis and the modeled DTP for Al/SiO_2/Si for offset DBB-FDTR. Similar to the case for focal DBB-FDTR, the DTP obtained by offset DBB-FDTR increases with increasing the offset between the pump and the probe beams. However, the thermal signal magnitude decreases by increasing the offset. Figure 3 shows that both focal and offset DBB-FDTR methods show phase sensitivity to important parameters of the particular sample of study (Al/SiO_2/Si). However, offset DBB-FDTR is more favorable when anisotropic heat transport is important [10, 12].

Results

Figure 4a shows the DTP for Al/SiO_2/Si measured by focal DBB-FDTR. The in situ measured rms spot sizes are 1.45 μm and 2.3 μm for the first and for the second focal positions, respectively. The fit resulted in the Al/SiO_2 thermal boundary conductance (TBC) of 87.6 ± 15 MW/m^{2}K and SiO_2/Si TBC of 28.2 ± 2.25 MW/m^{2}K, which are consistent with values reported previously [19-21]. Using focal DBB-FDTR, the TBC of the Al/Si sample has been measured to be 192.5 ± 10 MW/m^{2}K (Figure 4b), which is in agreement with the values reported in the literature [22, 23]. Focal DBB-FDTR was used to measure the TBC of Al/MgO as well as the thermal conductivity of MgO. Figure 4c shows the obtained fit and the measured DTP which resulted in Al/MgO

TBC of 163.8 ± 9.95 MW/m^{2}K and λ_{MgO} of 55.3 ± 11.2 W/mK. The results are consistent with the values reported in the literature [24].

Moreover, the results for offset DBB-FDTR with 1.5 μm pump-probe offset for Al/SiO_2/Si indicated TBCs of 63.2 ± 26 MW/m^{2}K for Al/SiO_2 and 33.3 ± 10.6 MW/m^{2}K for SiO_2/Si (Figure 5a) which are consistent with the results obtained from focal DBB-FDTR.

By comparing the results of focal and offset DBB-FDTR on the Al/SiO_2/Si sample (Figure 4a and Figure 5a), one can see that the results obtained from the focal DBB-FDTR measurement are considerably more accurate and less noisy than those obtained by the offset DBB-FDTR. We attribute the inaccuracy in the offset DBB-FDTR measurement to the limited repeatability of the actuator. Due to the randomness in the reference phase obtained from the analog signal generator every time a new frequency is set, the thermal phase is measured at two different offset points at each frequency (rather than making two measurements as function of frequency at two beam offset values). Therefore, the actuator is activated twice at each frequency point to take two measurements at different offset values. Our calibration showed that to obtain a 1 μm offset between the pump and probe beams, the actuator needs to be moved by 6 μm, while the repeatability of the actuator is limited to ±0.5 μm. In order to show the effectiveness of the offset DBB-FDTR technique while minimizing the error introduced by the limited repeatability of the actuator, two thermal FDTR measurements (without heterodyning) at two different offset values were performed up to 50 MHz. Since these measurements used the lock-in amplifier as signal source, each FDTR curve as function of frequency was measured separately, and the actuator was used only once. By subtracting the two phases measured, the instrumental contributions to the recorded phase were canceled (as described in DBB-FDTR Implementation section). Figure 5b shows the DTP measured for Al/SiO_2/Si and the obtained fits for two different offset values. This resulted in fitted SiO_2/Si TBC values of 29.8 ± 4.5 MW/m^{2}K and 30 ± 4.2 MW/m^{2}K for 1 μm and 1.5 μm offsets, respectively; which are consistent with those obtained from DBB-FDTR. However, for the measurements of Figure 5b, the sensitivity to Al/SiO_2 TBC is too small within the frequency range measured with FDTR, and a high-frequency approach such as DBB-FDTR is necessary (see Figure 3d). By comparing the results obtained from offset DBB-FDTR and offset differential FDTR (Figure 5a and 5b, respectively), one can see that the repeatability issues of the actuator have been eliminated.

Lastly, Figure 6 shows the thermal phase measured using FDTR extended up to 90 MHz before and after the noise correction using the mathematical approach described in the DBB-FDTR Implementation section.

Both focal and offset DBB-FDTR approaches are capable of identifying thermophysical properties at sub-micron length scales. This is achieved by the reduction of spot size and by decreasing the thermal penetration depth of heat carriers through increasing the frequency range of thermoreflectance measurements. Any frequency dependence in the thermophysical parameters originating from non-diffusive heat transport can be studied using such high-frequency systems [21]. An example was presented by Regner and co-workers who showed frequency dependence (i.e. heat carrier mean free path spectra) of thermal conductivity of Si [13, 14]. The interpretation of these results however depends on knowledge of non-diffusive heat conduction mechanisms [16, 25], and is a subject worthy of study, as it closely relates to how heat is transported in nanoscale systems. The samples studied in this work were not susceptible to the observation of frequency dependence in the thermal conductivity, as described below.

Firstly, we used Al transducers, and given the high electron-phonon coupling in Al, it is safe to neglect electron and phonon non-equilibrium effects within the transducer [25, 26]. For the Al/SiO_2/Si sample, the thick SiO_2 layer prevents the heat from reaching the Si layer, and given the disordered amorphous structure of SiO_2, only phonons of MFP ~1 nm are expected to contribute to its overall thermal conductivity [27]. Therefore, since the MFP in SiO_2 are much smaller than the shortest thermal penetration depth and spot size used in this experiment (~40 nm and ~1 μm, respectively), only diffusive transport is expected, yielding bulk-like thermophysical properties. For the Al/Si sample, the presence of the native <10 nm oxide layer causes the phonon spectral heat flux injected in the Si layer to be filtered in such a way that the apparent thermal conductivity of Si matches that of the bulk [28]. This is opposite to the work of Wilson and Cahill, where the oxide layer was removed, allowing for the full phonon spectrum to penetrate the Si substrate and yielding a frequency and spot size dependence to the apparent thermal conductivity data [25].

In the case of the MgO sample, the high modulation frequencies used in this work lead to thermal penetration depths as low as 200 nm. This, as well as the small spot sizes used, may lead to non-diffusive transport that manifests itself through an apparent thermal conductivity that is lower than the expected value. Wilson and Cahill report a lower apparent thermal conductivity for the Al/MgO system with spot

sizes of ~1 μm, and calculate a thermal conductivity accumulation function for MgO yielding ~75% of the bulk conductivity for phonon MFP up to ~300 nm [29]. We have calculated the thermal conductivity accumulation function of MgO from first principles and find that, contrary to ref. 29, phonons with MFP of ~200 nm contribute >90% of the thermal conductivity (see appendix). This indicates that at our experimental modulation frequencies we may be at the cusp of detecting non-diffusive transport in this system. Given that a diffusive model does not fit our experimental data very closely, a non-diffusive model may be needed to assess non-diffusive transport in this case, but this is out of the scope of this work. The data by Wilson and Cahill indicates that the non-diffusive effects in Al/MgO are much weaker than those in Al/Si [29].

Conclusion

In conclusion, two methods to extend FDTR were proposed to perform high frequency measurements of the thermophysical properties of submicron films (Figure 2b and 2c). Both methods eliminate the need to use expensive electro-optic modulators. By recovering the thermal phase obtained by a measurement either at a different focal point or at a different offset between pump and probe, a differential thermal phase is extracted. The two methods were used to extract thermal properties of different samples (Figure 4 and 5) and are suitable to study non-equilibrium dynamics of heat carriers in nanoscale systems.

Acknowledgments

M.S., M.R., and S.P. wish to acknowledge the Natural Sciences and Engineering Research Council of Canada and York University for financial support, as well as the facilities of the Shared Hierarchical Academic Research Computing Network (SHARCNET) and Compute Canada.

References

1. D. G. Cahill, H. E. Fischer, T. Klitsner, E. Swartz and R. Pohl, Journal of Vacuum Science & Technology A: Vacuum, Surfaces, and Films **7** (3), 1259-1266 (1989).
2. D. G. Cahill, Review of scientific instruments **61** (2), 802-808 (1990).
3. C. Dames, Annual Review of Heat Transfer **16** (16) (2013).
4. C. Monachon, L. Weber and C. Dames, Annual Review of Materials Research **46**, 433-463 (2016).

5. A. Ziabari, P. Torres, B. Vermeersch, Y. Xuan, X. Cartoixà, A. Torelló, J.-H. Bahk, Y. R. Koh, M. Parsa and D. Y. Peide, Nature communications **9** (1), 255 (2018).
6. A. J. Schmidt, R. Cheaito and M. Chiesa, Review of scientific instruments **80** (9), 094901 (2009).
7. A. J. Schmidt, R. Cheaito and M. Chiesa, Journal of Applied Physics **107** (2), 024908 (2010).
8. J. Yang, C. Maragliano and A. J. Schmidt, Review of Scientific Instruments **84** (10), 104904 (2013).
9. J. Yang, E. Ziade, C. Maragliano, R. Crowder, X. Wang, M. Stefancich, M. Chiesa, A. K. Swan and A. J. Schmidt, Journal of Applied Physics **116** (2), 023515 (2014).
10. J. P. Feser and D. G. Cahill, Review of Scientific Instruments **83** (10), 104901 (2012).
11. D. Rodin and S. K. Yee, Review of Scientific Instruments **88** (1), 014902 (2017).
12. M. Rahman, M. Shahzadeh, P. Braeuninger-Weimer, S. Hofmann, O. Hellwig and S. Pisana, Journal of Applied Physics **123** (24), 245110 (2018).
13. K. Regner, S. Majumdar and J. A. Malen, Review of Scientific Instruments **84** (6), 064901 (2013).
14. K. T. Regner, D. P. Sellan, Z. Su, C. H. Amon, A. J. McGaughey and J. A. Malen, Nature communications **4**, 1640 (2013).
15. J. P. Freedman, J. H. Leach, E. A. Preble, Z. Sitar, R. F. Davis and J. A. Malen, Scientific reports **3** (2013).
16. K. Regner, A. J. McGaughey and J. A. Malen, Physical Review B **90** (6), 064302 (2014).
17. D. G. Cahill, Review of scientific instruments **75** (12), 5119-5122 (2004).
18. A. J. Schmidt, X. Chen and G. Chen, Review of Scientific Instruments **79** (11), 114902 (2008).
19. P. E. Hopkins, J. R. Serrano, L. M. Phinney, S. P. Kearney, T. W. Grasser and C. T. Harris, Journal of Heat Transfer **132** (8), 081302 (2010).
20. C. Zhang, W. Zhao, K. Bi, J. Ma, J. Wang, Z. Ni, Z. Ni and Y. Chen, Carbon **64**, 61-66 (2013).
21. J. A. Malen, K. Baheti, T. Tong, Y. Zhao, J. A. Hudgings and A. Majumdar, Journal of Heat Transfer **133** (8), 081601 (2011).
22. A. J. Minnich, J. Johnson, A. Schmidt, K. Esfarjani, M. Dresselhaus, K. A. Nelson and G. Chen, Physical review letters **107** (9), 095901 (2011).
23. P. E. Hopkins, ISRN Mechanical Engineering **2013** (2013).
24. A. Giri, S. H. Wee, S. Jain, O. Hellwig and P. E. Hopkins, Scientific reports **6**, 32077 (2016).
25. R. Wilson and D. G. Cahill, Nature communications **5**, 5075 (2014).
26. C. Hua, X. Chen, N. K. Ravichandran and A. J. Minnich, Physical Review B **95** (20), 205423 (2017).
27. R. Zeller and R. Pohl, Physical Review B **4** (6), 2029 (1971).
28. C. Hua and A. J. Minnich, Physical Review B **97** (1), 014307 (2018).
29. R. Wilson and D. G. Cahill, Applied Physics Letters **107** (20), 203112 (2015).
30. P. Giannozzi, S. Baroni, N. Bonini, M. Calandra, R. Car, C. Cavazzoni, D. Ceresoli, G. L. Chiarotti, M. Cococcioni and I. Dabo, Journal of physics: Condensed matter **21** (39), 395502 (2009).
31. A. Jain, S. P. Ong, G. Hautier, W. Chen, W. D. Richards, S. Dacek, S. Cholia, D. Gunter, D. Skinner and G. Ceder, Apl Materials **1** (1), 011002 (2013).
32. A. Togo, F. Oba and I. Tanaka, Physical Review B **78** (13), 134106 (2008).
33. Available at https://bitbucket.org/sousaw/thirdorder.git
34. J. Carrete, B. Vermeersch, A. Katre, A. van Roekeghem, T. Wang, G. K. Madsen and N. Mingo, Computer Physics Communications **220**, 351-362 (2017).
35. K. Esfarjani, G. Chen and H. T. Stokes, Physical Review B **84** (8), 085204 (2011).

Appendix

The thermal conductivity accumulation functions of Si and MgO were calculated through the Boltzmann transport equation using phonon dispersions and scattering rates obtained by *ab initio* density functional theory (DFT).

The phonon interatomic force constants are calculated through Qunatum Espresso [30] using the projector augmented-wave (PAW) method using Perdew-Burke-Ernzerhof pseudopotentials. The crystals were modeled starting from the relaxed lattice constants [31] using a 10x10x10 Monkhorst-Pack wavevector grid. The wavefunction kinetic energy cut-off value was checked by monitoring the convergence of the system's total energy. Coulomb interactions were taken into account by computing Born effective charges. The second-order force constants were extracted using the package Phonopy [32]. Third-order force constants were extracted with a 3x3x3 supercell using the package Thirdorder [33]. Finally, the thermal conductivity accumulation functions are calculated via the almaBTE package [34] using a 24x24x24 wavevector grid, which includes energy and wavevector specific scattering rates and isotopic scattering.

The results for Si and MgO are shown in Figure 7. The accumulation for Si follows closely the dependence previously reported [35]. The accumulation for MgO shows a faster saturation at lower phonon mean free paths as compared to the curve reported in ref. 29, but we note that one source for the difference is that the calculation reported here uses phonon scattering rates determined from first principles calculations, whereas in ref. 29 phonon scattering rates are modeled analytically through a frequency-dependent power law.

Figures

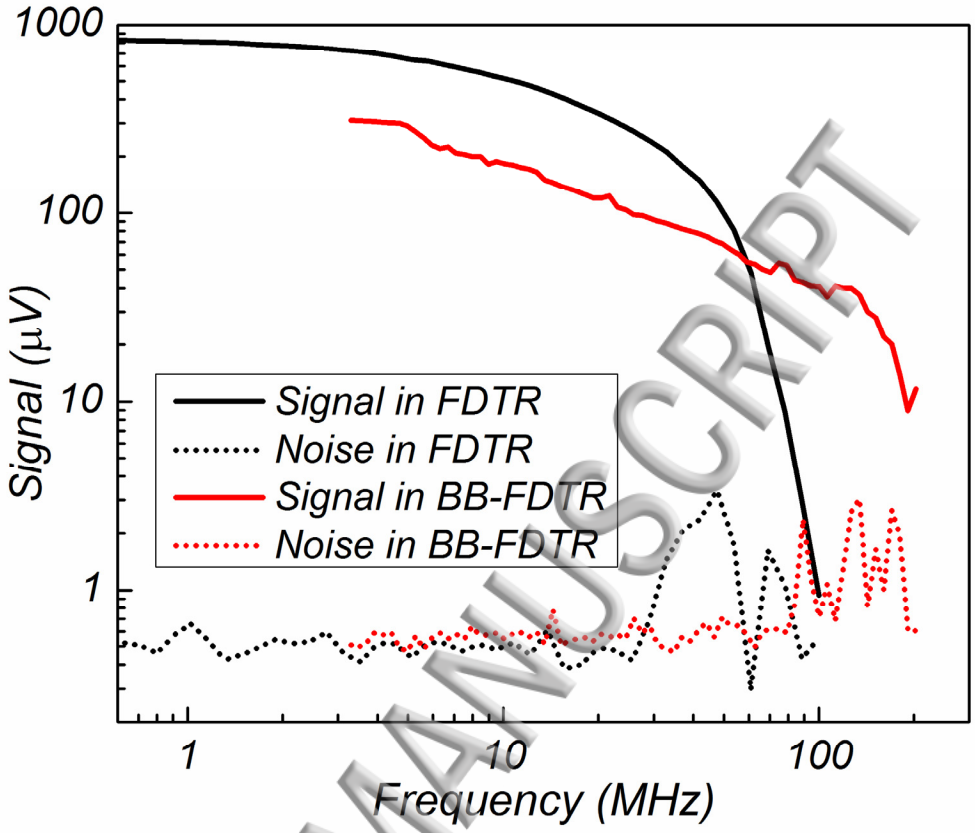

Figure 1. A comparison between strength of thermal signal and noise in a typical FDTR measurement and a BB-FDTR measurement.

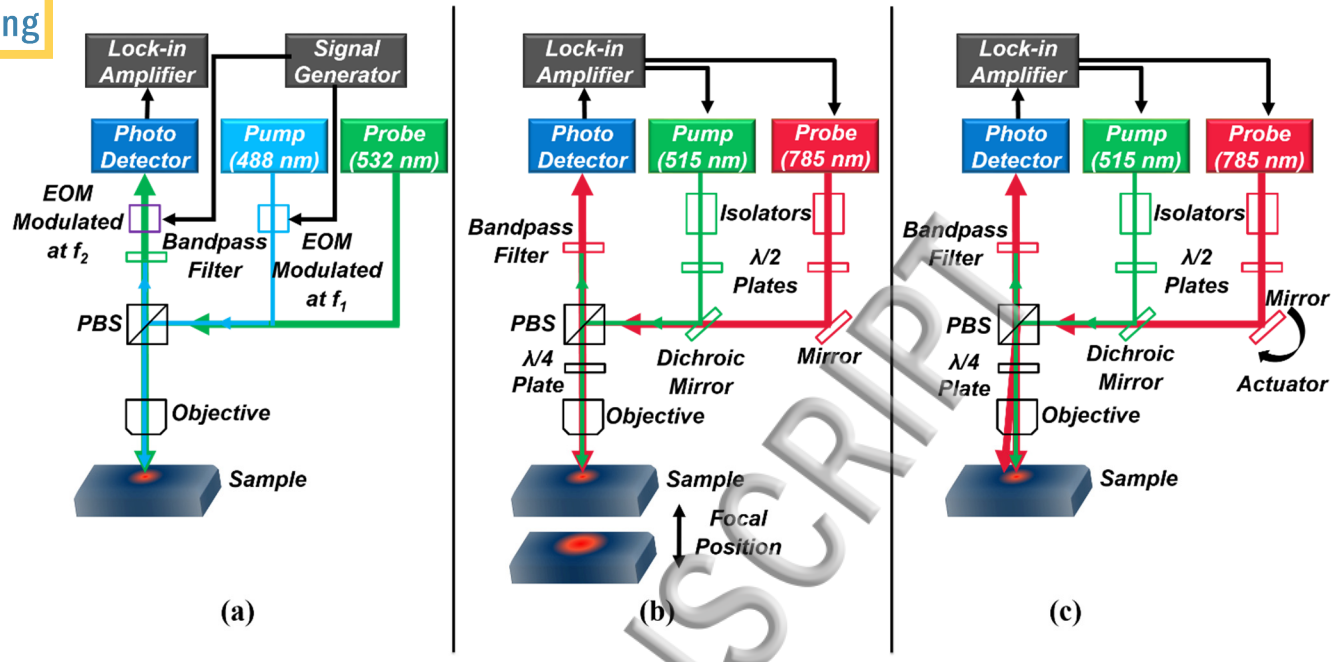

Figure 2. (a) Regner's BB-FDTR configuration. (b) DBB-FDTR configuration described in this work based on changing the focal point, and (c) based on changing the offset between pump and probe.

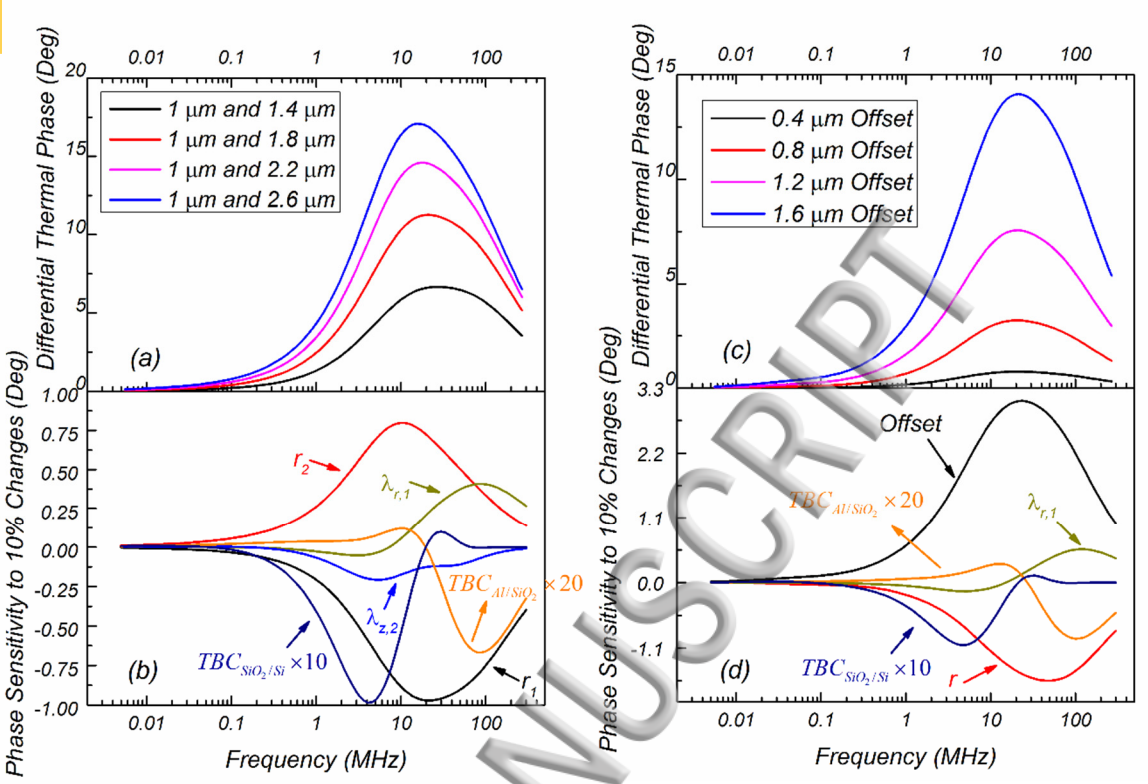

Figure 3. Modeled response of DBB-FDTR signals. For all the curves above, the sample is Al(59)/SiO_2(150)/Si. (a) Modeled DTP in focal DBB-FDTR for different pairs of rms spot sizes. The larger the amount of defocus, the larger is the resulting rms spot size, though the associated signal will be lower. (b) Sensitivity of DTP with respect to 10% changes in different parameters. r_1 and r_2 are the rms value of pump and probe spot sizes at two focal positions. $\lambda_{r,1}$ is the radial thermal conductivity in the Al layer, TBC is the thermal boundary conductance, and $\lambda_{z,2}$ is the perpendicular thermal conductivity of SiO_2. (c) Modeled DTP in offset DBB-FDTR for different pump-probe beam offset values. (d) Sensitivity of DTP with respect to 10% changes in different parameters. r and Offset are the rms value of pump and probe spot sizes, and the offset between pump and probe beams, respectively.

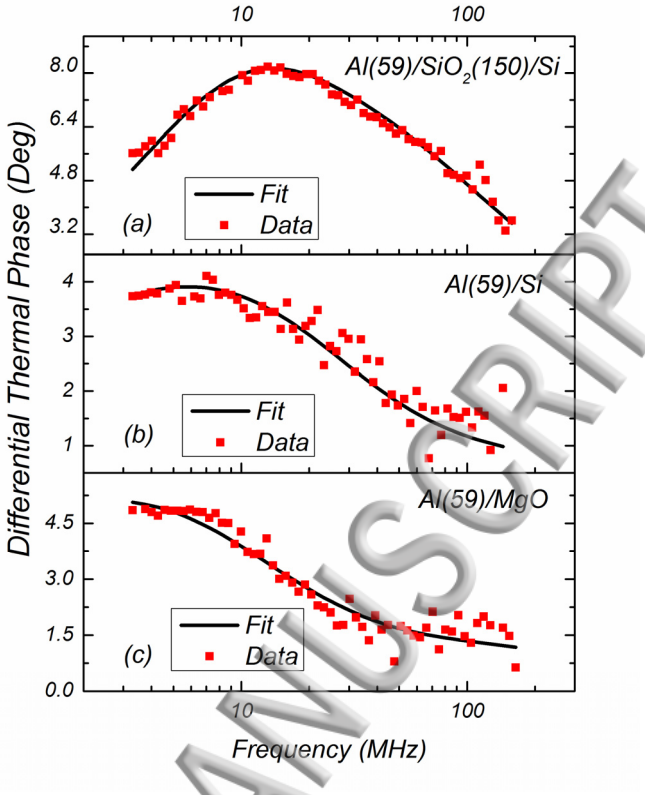

Figure 4. Measured DTP (squares) and the obtained fit (lines) for (a) Al/SiO2/Si, (b) Al/Si, and (c) Al/MgO, obtained by focal DBB-FDTR.

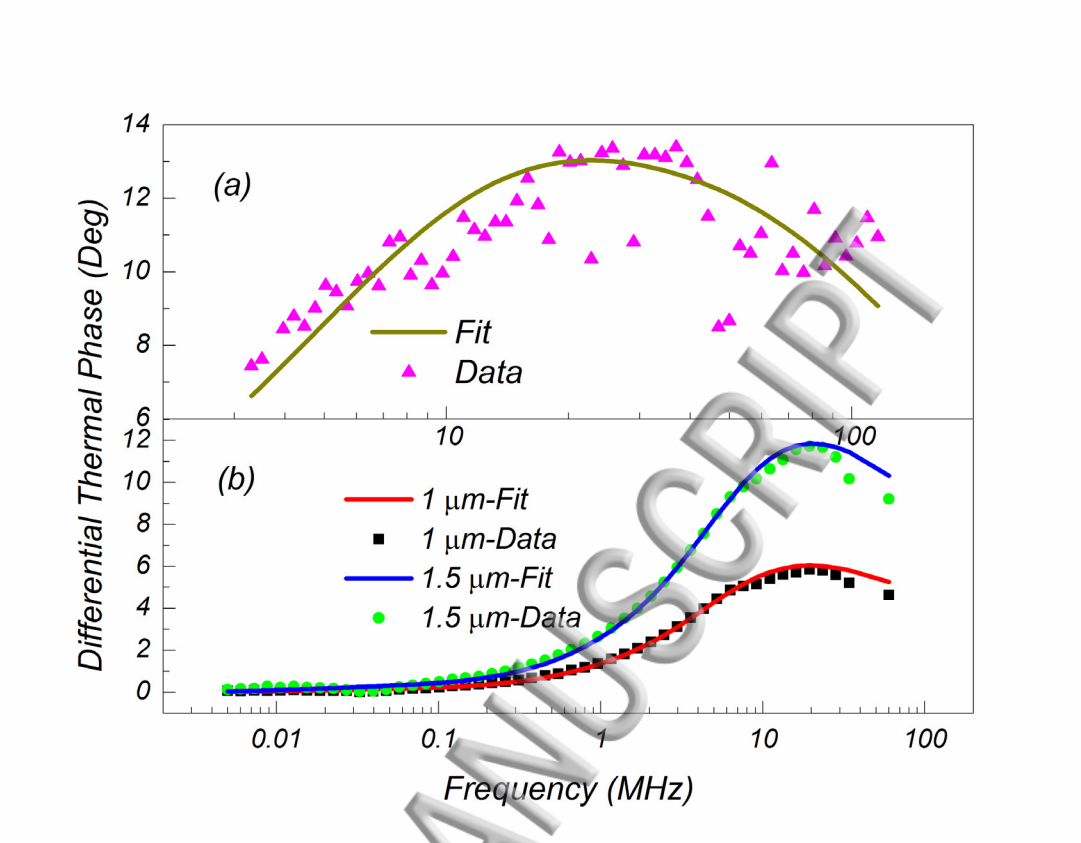

Figure 5. (a) Measured DTP (triangles) and the obtained fit (line) for Al/SiO_2/Si by offset DBB-FDTR with 1.5 μm pump-probe offset. (b) Measured DTPs (symbols) and the obtained fits (lines) in offset differential FDTR for the same sample, obtained at two different pump and probe offsets.

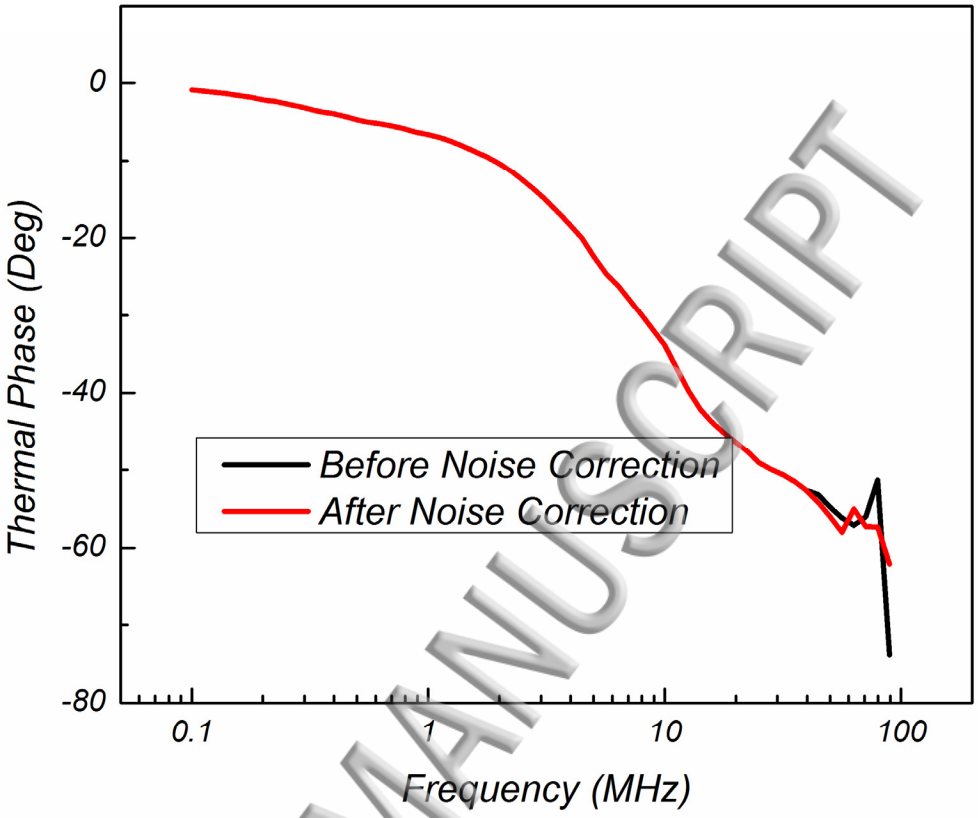

Figure 6. Extension of FDTR to 90 MHz; comparing the thermal phase before and after mathematical noise correction for Al/SiO_2/Si.

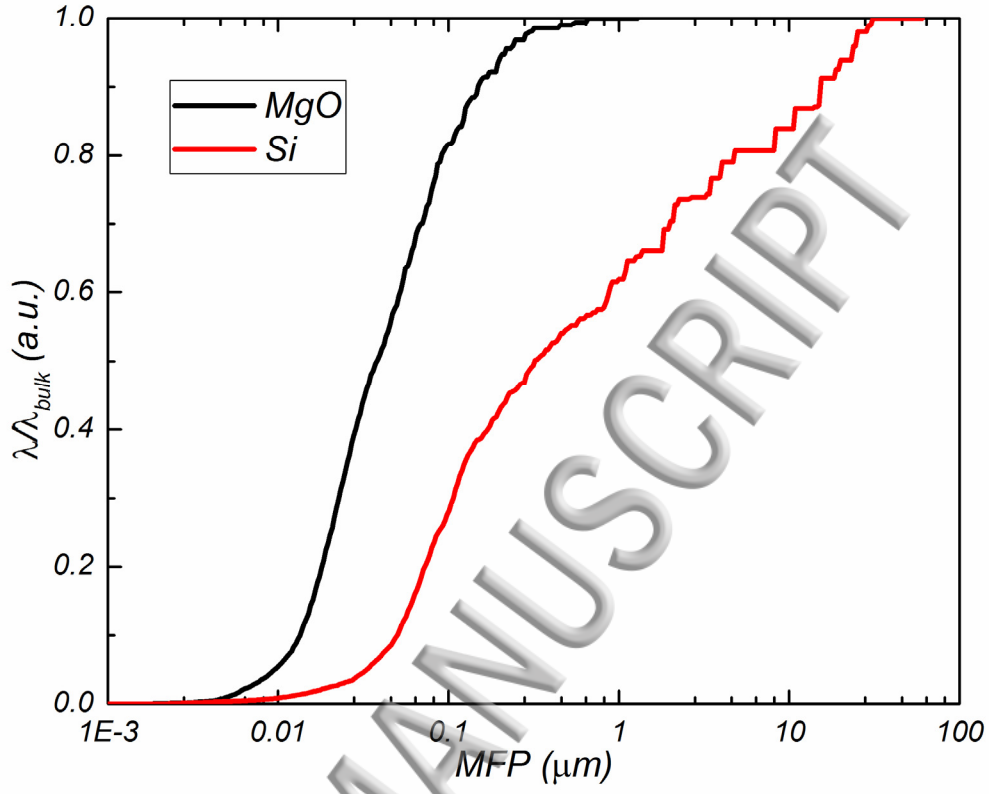

Figure 7. Thermal conductivity accumulation as function of phonon mean free path calculated via DFT.

Table 1. Thermophysical properties of the samples studied in this work. The values for the in-plane thermal conductivity of Al and film thickness are specific to our samples, all other values in the table are taken from the literature.

	λ_z (W/mK)	λ_r (W/mK)	C (MJ/m^{3}K)	d (nm)
Al	243	173	2.42	59
SiO_2	1.32	1.32	1.59	150
Si	145	145	1.64	Semi-infinite
MgO	Fit	Fit	3.37	Semi-infinite